fire

MDPI

Article

Thermogravimetric Assessment of Biomass: Unravelling Kinetic, Chemical Composition and Combustion Profiles

Roberto Paredes [1], Blanca Castells [2,3] and Alberto Tascón [4,5,*]

[1] Department of Geological and Mining Engineering, E.T.S. Ingenieros de Minas y Energía, Universidad Politécnica de Madrid, C/Ríos Rosas 21, 28003 Madrid, Spain; r.pgallo@upm.es
[2] Department of Energy and Fuels, E.T.S. Ingenieros de Minas y Energía, Universidad Politécnica de Madrid, C/Ríos Rosas 21, 28003 Madrid, Spain
[3] Laboratorio Oficial José María de Madariaga (LOM) & Technological Center TECMINERGY, TecnoGetafe, 28906 Madrid, Spain
[4] Department of Agriculture and Food Science, Universidad de La Rioja, C/Madre de Dios 53, 26006 Logroño, Spain
[5] CIVA Research Center, Universidad de La Rioja, 26006 Logroño, Spain
* Correspondence: alberto.tascon@unirioja.es

Abstract: Thermogravimetric analysis (TGA) was performed on six samples of pine wood, poplar sawdust and olive residue, and the kinetic parameters were evaluated by using isoconversional models. The hemicellulose, cellulose and lignin contents were also estimated using the Fraser–Suzuki deconvolution method. In addition, a range of thermodynamic parameters and combustion indices was calculated. Significant correlations were found between the kinetic, thermodynamic and combustion parameters. The ignition index showed an inverse relationship with the activation energy, whereas the burnout index correlated with enthalpy values for most samples. Higher heating rates during TGA increased ignition and combustion efficiencies but decreased combustion stability. Differences in behaviour were detected between the olive residues, which had a much higher lignin content (51.2–56.9%), and the woody biomass samples (24.2–29.2%). Moreover, the sample with the highest ash content also exhibited some distinctive characteristics, including the lowest high heating value and ignition index, coupled with the highest activation energy, indicating a less favourable combustion behaviour than the other samples. The particle size of the samples was also found to be critical for both combustion efficiency and safety.

Keywords: biomass; solid biofuels; thermogravimetric analysis; combustion kinetics; entropy; enthalpy; combustion behaviour; pine wood; poplar sawdust; olive waste

check for updates

Citation: Paredes, R.; Castells, B.; Tascón, A. Thermogravimetric Assessment of Biomass: Unravelling Kinetic, Chemical Composition and Combustion Profiles. *Fire* **2024**, *7*, 396. https://doi.org/10.3390/fire7110396

Academic Editor: Thomas H. Fletcher

Received: 4 September 2024
Revised: 23 October 2024
Accepted: 26 October 2024
Published: 31 October 2024

Copyright: © 2024 by the authors. Licensee MDPI, Basel, Switzerland. This article is an open access article distributed under the terms and conditions of the Creative Commons Attribution (CC BY) license (https://creativecommons.org/licenses/by/4.0/).

1. Introduction

In the last few decades, climate change has become one of the main concerns of society. The melting of the poles, changes in ecosystems, reduction of biodiversity and several other devastating natural disasters [1,2] are a consequence of greenhouse gas (GHG) emissions, which have increased steadily since the Industrial Revolution [1,2]. In this context, many governments have come together in summits and agreements to jointly respond to this challenge. In particular, three action plans were agreed upon in the European Union for transition to a climate-neutral society for 2020, 2030 and 2050. The latter is expected to achieve a net zero greenhouse gas emission economy [3,4].

In this scenario, renewable energies have become a key factor in reducing energy dependence on fossil fuels [5]. However, finding a viable substitute for fossil fuels is not an easy task, since many renewable energy sources depend on external factors that prevent them from meeting peak demand. In this context, biofuels can play an important role as they have similar production characteristics to fossil fuels: their generation is not

dependent on the weather, and they can be delivered in different states of matter, such as biogas, biodiesel or bioethanol, and solid biofuels [3,6].

The use of solid biofuels is a wise choice in this scenario of global climate emergency because biomass releases biogenic carbon dioxide (CO_2), which makes biomass conversion processes carbon neutral [7]. Therefore, if managed in a sustainable way, bioenergy can achieve significant reductions in net emissions [8,9]. Moreover, solid biofuels have a high benefit–cost ratio, as they are low-cost raw materials and they also have the potential to improve the energy mix owing to their high versatility and flexibility [10,11]. However, the bioenergy sector faces several challenges [12], including the complexity of supply chains, the low bulk density of many raw materials or wide variation in feedstock characteristics. Moreover, the high moisture content and low energy density of many biomass materials represent a limitation. In addition, some materials have high ash and chlorine content, which causes problems with the formation of deposits and corrosion, respectively [12].

Depending on its composition, biomass can be treated by different conversion processes [12–14]. These are divided into two large groups: thermochemical and biochemical processes. The former includes combustion, gasification and pyrolysis, while the latter includes anaerobic digestion and fermentation [15–18]. Not only do these energy conversion processes need to be correctly selected, designed and managed, but so also do the pre-treatments for upgrading raw materials, along with corresponding storage, handling and transportation operations [19].

Furthermore, the handling and processing of solid biofuels present associated risks that need to be managed. Understanding the kinetic, thermodynamic and combustion profiles is essential not only to optimise their use but also to minimise fire, smouldering and explosion risks [20,21].

The kinetic parameters of biomass can be obtained by thermogravimetric analysis (TGA) through the study of corresponding curves [22]. The methods for carrying out this study can be classified into three main groups. The first group involves the assumption of the kinetic model, such as the Coats–Redfern or the Freeman–Carroll methods [23]. The second group consists of linear isoconversional methods that calculate the kinetic parameters without applying the assumption of the reaction model, such as the Friedman, Kissinger–Akahira–Sunose (KAS) or Flynn–Wall–Ozawa (FWO) methods. These isoconversional methods are more accurate, since they eliminate the dependence of the kinetic parameters on the reaction model [24,25]. Finally, the third group involves an increasing and sinusoidal heating schedule, i.e., modulated thermogravimetry. However, these last methods present complex calculations which hinder their application.

Due to the relevant information provided by thermogravimetric analysis applying these kinetic methods, several authors have focused on defining the kinetic parameters of biomass conversion processes, such as combustion or pyrolysis. Chen et al. [26] carried out studies to evaluate the thermodynamic parameters to gain a better understanding of the energy transformations involved in the thermal degradation of solid biomass. Additionally, they conducted analyses of combustion parameters to determine the indicators of combustion efficiency, ignition propensity and combustion stability in solid biofuels. However, the values for woody biomass can significantly change depending on the type of biomass. The literature shows activation energies in the range of 120 to 170 kJ/mol for pine samples [27–30], although some authors have reported greater values, even over 200 kJ/mol [31]. On the other hand, research focused on olive waste is not as extensive, and activation energies are located between 130 and 300 kJ/mol [32–34]. Several authors have related activation energy values with the composition of lignocellulosic biomass [35,36], since the degradation of cellulose and hemicellulose defines the kinetic parameters [37–39].

In this context, deconvolution techniques can be applied to TGA data to determine fuel composition. Perejón et al. [37] tested different mathematical fitting functions and concluded that Fraser–Suzuki properly fits any kinetic curve no matter the kinetic model obeyed by the solid-state reaction. Previously published research has already demonstrated that the technique can provide accurate estimations of hemicellulose, cellulose and lignin

content [38,39]. The composition profile of lignocellulosic biomass is relevant, as it is known that each component presents differences during pyrolysis, ignition and combustion processes [40].

Moreover, TGA data provide meaningful information about how fuels may behave under different external conditions like heating rate or atmosphere composition. Such information is key to optimising large-scale conversion processes and predicting their performance over long-term use. In addition, TGA results can be related to other analytical techniques to obtain a complete picture of biomass thermal degradation mechanisms [41–43]. However, as mentioned earlier, large variations are found in the literature for the activation energy values of biomass materials. In addition, there seems to be a lack of standardised procedures related to the preparation of biomass samples and the conditions of TGA tests. Moreover, the influence of the particle size of the samples is unclear. The situation hinders the comparison of results for biomass samples between laboratories [44].

Although kinetic analysis is the most common research topic in TGA, other authors have focused on assessing the thermochemical parameters of biomass, such as enthalpy, entropy and Gibbs free energy, as well as combustion parameters, such as burnout or flammability indices [45,46]. These parameters provide valuable insights into the combustion behaviour, thermodynamic properties and overall quality of solid biofuels [47]. The use of these parameters to address optimal conversion processes remains necessary for complete knowledge of the process.

Indeed, there is a lack of comprehensive studies that thoroughly combine thermodynamic parameters, combustion indices and biomass composition (Fraser–Suzuki deconvolution) through TGA. The kinetics of biomass conversion processes has been widely studied but there are few studies that include a thermodynamic assessment, which can provide valuable insights into the conversion processes and their mechanisms. Although some studies have provided the combustion indices of biomass, it is important to correlate them with kinetic analysis to assess the complete process. Because of that, the objective of this study was to combine these three groups of properties with the kinetic analysis determined through thermogravimetry to obtain a complete profile of biomass materials that includes not only their potential as an energy source and the most convenient chemical conversion processes but also their self-heating and fire risks.

2. Materials and Methods

The experimental procedures and analytical techniques employed in the present study are explained below. Details are provided on the selection and preparation of the biomass samples; thermogravimetric analysis (TGA) methodology; mathematical models for data analysis, including the Fraser–Suzuki deconvolution method; and calculations of kinetic, thermodynamic and combustion parameters.

2.1. Biomass Samples

Four biomass materials were used in this present study (see Table 1). These materials can be classified as olive waste, which included olive pits and olive cake pellets, and woody biomass, which included pine pellets and poplar sawdust.

Table 1. Heating values (MJ/kg, dry basis) and proximate (wt%, dry basis) and ultimate (wt%, dry ash-free basis) compositions of the biomass materials.

Material	Origin	V	A	FC	C	H	N	O	S	Cl	HHV	LHV
Olive pits	Jaén, Spain	78.7	1.2	20.1	51.04	6.03	0.34	42.54	0.03	0.025	20.2	19.0
Olive cake pellets	Sevilla, Spain	74.3	7.2	18.5	51.29	6.24	1.49	40.72	0.10	0.162	18.9	17.7
Poplar sawdust	La Rioja, Spain	83.6	1.0	15.4	49.47	5.89	1.40	43.12	0.05	0.071	19.5	18.1
Pine pellets	León, Spain	82.2	0.3	17.5	50.67	6.13	0.09	43.07	0.02	0.02	20.3	19.0

Poplar sawdust is a typical waste produced in sawmills, while pine pellets are a commercially available biomass used as solid biofuel for heating systems. Olive pits—or olive stones—and olive cake are by-products of the industrial olive oil extraction process. The olive cake analysed in this study consisted of exhausted destoned olive cake pellets. After drying plus removing the pieces of olive stone, the solid residue from the mechanical extraction of olive oil (a two-phase process) was subjected to further chemical treatment with hexane to extract a second-quality oil; the resulting residue was pelletised to facilitate its handling and transport. Such pellets constitute the olive cake pellets considered here. These two olive samples have been previously studied regarding their ignition and explosion characteristics [34].

Proximate and ultimate analyses were performed with an oven (Memmert), a 367 PE muffle furnace (Selecta) and a CHNS Micro TruSpec analyser (LECO) by applying conventional techniques for coal characterisation. The proximate analysis was carried out following standards ASTM 3302 [48], UNE 32019 [49] and UNE 32004 [50] for the moisture (M), volatile matter (V) and ash (A) content, respectively; fixed carbon (FC) was estimated by difference. For the elemental analysis, American standard ASTM 5373 was followed for carbon, hydrogen and nitrogen [51], ASTM 4239 for sulphur [52] and ASTM 2361 for chlorine [53]; oxygen content was calculated by difference. In addition, higher (HHV) and lower (LHV) heating values were obtained with a 6300 Parr calorimeter following the UNE 32006 procedure [54]. Table 1 presents the results of all these analyses for the four biomass samples.

The pine pellets were milled (GME-1100C hammer mill, Garhé, Amorebieta, Spain) and sieved (electro-mechanical shaker, Controls, Milan, Italy) at the University of La Rioja. Three granulometric fractions were generated: fraction lower than 400 µm (PP400), fraction lower than 250 µm (PP250) and fraction lower than 80 µm (PP80). This experimental set up was designed to study the influence of particle size on the results. On the contrary, poplar sawdust (POP) was sieved (400 µm) but without any prior milling. The olive samples—olive pits and olive cake pellets (OPI and OCP, respectively)—were milled at LOM laboratory using an IKA-Werke M20 mill (Staufen, Germany) and later sieved with a 500 µm sieve.

Prior to the TGA experiments, the particle size distribution of the six samples was obtained by laser diffraction (Mastersizer 2000, Malvern Instruments Ltd, Worcestershire, UK) and the moisture content was determined by the measurement of mass reduction upon heating the sample to a temperature of 105 °C (Mettler Toledo HB43-S halogen analyser, Greifensee, Switzerland). Table 2 shows the main particle size parameters and the moisture content (M) of the six samples that were prepared from the four biomass materials, along with their nomenclature.

Table 2. Identification, particle size properties and moisture content of the samples.

Material	Sample	d_{10} (µm)	d_{50} (µm)	d_{90} (µm)	SSA (m^2/g)	$d_{[3,2]}$ (µm)	$d_{[4,3]}$ (µm)	M (%)
Olive pits	OPI	28.2	251.1	569.6	0.099	60.1	270.8	8.7
Olive cake pellets	OCP	37.0	223.5	519.9	0.073	81.7	253.4	8.2
Poplar sawdust	POP	20.7	134.1	499.5	0.136	44.2	209.5	6.2
Pine pellets	PP400	80.9	315.3	683.9	0.038	158.1	355.7	6.8
	PP250	36.8	169.6	406.1	0.074	80.8	200.7	7.4
	PP80	17.7	67.6	169.8	0.191	31.4	82.5	7.8

The particle size parameters d_{10}, d_{50} and d_{90} correspond to the particle diameter at which 10%, 50% and 90% of the sample's mass comprises particles with a diameter less than those values, respectively [55]. In addition, SSA provides the total surface area of particles per unit mass [56], while $d_{[3,2]}$ and $d_{[4,3]}$ correspond to surface-volume diameter (Sauter diameter) and volume-weighted diameter (De Brouckere diameter), respectively [57].

As can be seen, all samples were polydispersed, i.e., they presented a wide particle size distribution. The three PP samples showed decreasing diameter values and increasing SSA in accordance with the sieve size applied. Notably, the POP sample was the second-finest sample according to its SSA, d[3,2], d_{10} and d_{50} values, despite using a 400 µm sieve. From the results in Table 2, it can be noted that all materials presented d_{90} values greater than the corresponding sieve size used to prepare the samples. This fact can be explained by the fibrous nature of biomass particles. When milled, fibrous biomass presents elongated particles that can go through the sieve, since the dimension that is measured is the width [58]. Moreover, laser diffraction assumes spherical particles, introducing a significant degree of uncertainty. These controversies are explained in detail elsewhere [57].

2.2. Thermogravimetric Analysis

Thermogravimetric analysis (TGA) measures mass variations of a sample versus temperature. In the present research, a Mettler Toledo TG-DSC T50 apparatus was used together with 70 µL alumina crucibles. The tests were carried out controlling the atmosphere inside the furnace, the initial and final temperatures, and the heating rate (β). In this study, three heating rates were used: 5, 10 and 20 K/min. The initial and final temperatures were set to 30 °C and 800 °C, respectively. At the end of the test, an isothermal stage of 5 min at 800 °C was applied to ensure the complete reaction. The tests were performed using 79% of nitrogen and 21% of oxygen and a 5 mL/min air flow that simulated a combustion process.

From the TGA curves, the first derivative (DTG) was obtained to properly address the results of the analysis. Indeed, biomass samples typically lead to a curve in which three stages can be clearly identified [59,60]: drying process and intramolecular moisture release (approximately between ambient temperature and 120 °C); biomass degradation process (approximately between 120 °C and 500 °C), in which mainly hemicellulose and cellulose devolatilise; and oxidation of the carbonaceous residue (approximately between 500 °C and 800 °C).

Furthermore, from the TGA and DTG curves it is possible to define the temperature at which the maximum weight loss was produced (T_p) and the temperature at which the reactions accelerated, which is known as the induction temperature (*IT*) [61].

2.3. Fraser–Suzuki Deconvolution

Lignocellulosic biomass is composed of lignin, cellulose and hemicellulose. Therefore, after releasing the moisture content, the degradation of the sample corresponds to the devolatilisation of these three polymers. Hence, it is possible to estimate the composition of lignocellulosic samples by applying deconvolution to the DTG curve and calculating the area beneath each component curve [62–64]. Among the different methods for curve deconvolution, such as Gaussian, Lorentzian (with a symmetric function approach) and Fraser–Suzuki (with an asymmetric function approach) [37,38,65–68], the latter was selected due to its accuracy [38,69,70]. Equation (1) shows the mathematical model.

$$y = \sum_{i=1}^{n} h_i \times exp\left[-\frac{ln2}{s_i^2} ln\left(1 + 2s_i \frac{T - p_i}{w_i}\right)^2\right] \quad (1)$$

where y is the deconvoluted curve, h_i is the weight of the ith-curve over the total curve, s_i the skewness or asymmetry of the ith-curve, p_i is the mean value of the ith-curve, w_i is the width of the ith-curve and T is the absolute temperature. Moreover, n represents the number of pseudocomponents that are obtained from the deconvolution process. Typically, it is set at 3 to obtain hemicellulose, cellulose and lignin. However, some samples might produce a carbonaceous residue or char at the end of the reaction, leading to a fourth component [38,69]. In the present study, three pseudocomponents were considered.

2.4. Combustion Indices

To assess the combustion behaviour of the six samples under investigation, several combustion indices based on the TGA data previously obtained were calculated, as reported in Table 3. R_p is the maximum weight-loss rate (%/min); R_v is the average mass-loss rate (%/min); IT, as previously mentioned, is the induction temperature (°C); T_b is the burnout temperature (°C), taken as the point immediately before reaction ceases when the rate of weight loss is 1%/min [47]; T_p is the peak temperature (°C); t_p is the peak time (min); t_i is the induction temperature time (min); $\Delta t_{1/2}$ is the time to reach half of the maximum burning rate (min); and t_b is the burnout time (min).

Table 3. Combustion indices, their expressions and references.

Combustion Index	Equation	
Ignition index [71]	$D_i = \frac{-R_p}{t_i \times t_p}$	(2)
Burnout index [71]	$D_b = \frac{-R_p}{\Delta t_{1/2} \times t_i \times t_b}$	(3)
Comprehensive combustion index [71]	$S = \frac{(-R_p) \times (-R_v)}{IT^2 \times T_b}$	(4)
Flammability index [72]	$C = \frac{-R_p}{IT^2}$	(5)
Combustion intensity index [71]	$H_f = T_p \times ln\left(\frac{\Delta t_{1/2}}{-R_v}\right)$	(6)
Combustion stability index [71]	$D_w = \frac{-R_p}{IT \times T_p}$	(7)

Both ignition (D_i) [73–75] and burnout (D_b) [73–76] indices indicate the efficiency of the reaction, as the first is related to volatile content and the second to energy release during the process. On the other hand, the comprehensive combustion index (S) explains fuel combustion performance [73–75]. The flammability index (C) [77] and the combustion stability index (D_w) [78] provide information regarding the evolution of the combustion. Finally, the combustion intensity index (H_f) defines the energy rate of the process [79].

2.5. Kinetic Models

In the present study, three model-free or isoconversional methods were chosen, since they provide more accurate results than the data-fitting kinetic models, as explained above. The selected methods were the Friedman, Kissinger–Akahira–Sunose (KAS) and Flynn–Wall–Ozawa (FWO) methods. The KAS and FWO models were selected due to their robustness against errors compared to the differential isoconversional methods like the Friedman method [16]. Isoconversional methods allow the determination of kinetic parameters without assumptions about the reaction mechanism, and they define the thermochemical conversion rate by Equation (8) [80]:

$$\frac{d\alpha}{dt} = k(t) f(\alpha) \tag{8}$$

where α represents the dimensionless conversion degree (see Equation (9)), t is time, $k(t)$ is the reaction rate constant defined using Arrhenius law (see Equation (10)) and $f(\alpha)$ is the reaction model.

$$\alpha = \frac{m_0 - m_t}{m_0 - m_f} \tag{9}$$

$$k(t) = A\, exp\left(-\frac{Ea}{RT}\right) \tag{10}$$

where m_0 (mg) is the initial mass, m_t (mg) is the mass at a certain time t, m_f (mg) is the final mass, A (min^{-1}) is the pre-exponential factor, Ea ($J \times mol^{-1}$) is the activation energy, R is the universal gas constant (8.314 $J \times K^{-1} \times mol^{-1}$) and T (K) is the absolute temperature.

Considering that the heating rate can be defined as $\beta = dT/dt$, Equation (8) can be rewritten as Equation (11).

$$\frac{d\alpha}{dT} = \frac{A}{\beta} exp\left(-\frac{Ea}{RT}\right) f(\alpha) \tag{11}$$

2.5.1. Friedman Method

The Friedman method [81] is a differential method that assumes that the reaction model remains constant, so degradation depends on the mass-loss rate. Equation (12) represents the Friedman method equation and can be obtained applying logarithms to Equation (11):

$$ln\left(\beta\frac{d\alpha}{dt}\right) = ln[Af(\alpha)] - \frac{Ea}{RT} \tag{12}$$

When plotting $ln(d\alpha/dt)$ vs. $1/T$ for each heating rate, a straight line is obtained whose slope is proportional to the activation energy.

2.5.2. Kissinger–Akahira–Sunose (KAS) Method

The KAS method [82] is an integral method that applies an approximation of $P(x) = x^{-2}\, e^{-x}$ to the rate equation. If the integral form of Equation (11) is expressed as shown in Equation (13), where $g(\alpha)$ is the integral form of the reaction model, the KAS method can be defined by Equation (14).

$$g(\alpha)\int_0^{\alpha}\frac{d\alpha}{f(\alpha)} = \frac{A}{\beta}\int_0^{T} e^{-\frac{Ea}{RT}}dT = \frac{AEa}{\beta R}P(x) \tag{13}$$

$$ln\left(\frac{\beta}{T^2}\right) = ln\frac{AR}{Eag(\alpha)} - \frac{Ea}{RT} \tag{14}$$

When plotting $ln(\beta/T^2)$ vs. $1/T$, the slope of the straight line obtained is proportional to the activation energy.

2.5.3. Flynn–Wall–Ozawa (FWO) Method

The FWO [83] method is similar to the KAS method, but the approximation to the rate equation differs, leading to Equation (15).

$$ln(\beta) = ln\frac{AEa}{Rg(\alpha)} - 5.331 - 1.052\frac{Ea}{RT} \tag{15}$$

In this method, the slope of the straight line obtained when plotting $ln(\beta)$ vs. $1/T$ is proportional to activation energy, and its intercept is $ln(A \times Ea)/R$.

2.6. Thermodynamic Parameters

Once activation energy is defined, it is possible to estimate some crucial thermodynamic parameters, such as enthalpy (ΔH), Gibbs free energy (ΔG) and entropy (ΔS). To do so, it is necessary to define the pre-exponential factor as a kinetic parameter. Isoconversional methods require a model assumption for the pre-exponential factor determination, so Equation (16) reported in Table 4 has been used in the present study [84].

Table 4. Kinetic and thermodynamic parameters.

Parameters	Equations	
Pre-exponential factor, A (1/s)	$A = \left[\beta \times E_\alpha \times exp\left(\frac{E_a}{R\times T_p}\right)\right]/(R \times {T_p}^2)$	(16)
Enthalpy, ΔH (kJ/mol)	$\Delta H = E_a - (R \times T)$	(17)
Gibbs free energy, ΔG (kJ/mol)	$\Delta G = E_a + R \times T_p \times ln\,[(K_B \times T_p)/(h \times A)]$	(18)
Entropy, ΔS (kJ/mol×K)	$\Delta S = \frac{\Delta H - \Delta G}{T_p}$	(19)

Table 4 shows the equations applied to calculate the thermodynamic parameters in this study [85]. It must be noted that, since they depend on activation energy, three values of each parameter were obtained, one per each isoconversional method. Moreover, the equations show dependence on β and T_p, so the average of these values was used.

In Table 4, K_B represents the Boltzmann constant with a value of 1.381×10^{-23} J/K, h denotes the Planck constant with a value of 6.626×10^{-34} J·s, T represents the absolute temperature in Kelvin (K) and, again, T_p stands for the peak temperature observed on the DTG curve in Kelvin (K).

3. Results and Discussion

The findings from the thermogravimetric analysis, biomass composition estimates and calculated combustion indices are presented and analysed in this section. The kinetic and thermodynamic parameters derived from the experimental data are also discussed, highlighting correlations between the different variables. Comparisons are drawn with the relevant literature to contextualise the results. In addition, the influence of the biomass type, particle size and heating rate on the combustion behaviour and thermal degradation processes is examined.

3.1. TGA Results

The results obtained from the thermogravimetric analysis are presented in Figures S1–S6 of the Supplementary Materials, where both the TGA and DTG curves are plotted for each sample and heating rate. These results showed important differences between the two main types of biomass considered in this study.

Figures S1–S6 also show the residue that remains after the combustion process, which is composed mainly of carbonaceous matter and ashes. Almost every curve led to 20% of residue, but the OCP sample had a value greater than OPI—and greater than the rest of samples—with around 30%; these results are consistent with the previous literature, as olive cake has a much higher amount of ash than olive pits (see Table 1) [34]. In addition, it is important to note that the OPI sample led to almost no residue when the heating rate was set at 5 K/min. This fact means that the heating rate was sufficiently low for that sample to not produce thermal lag and, therefore, the residue corresponded mainly to ash, which is typically around 1–2% [34,86]. A similar behaviour was found in PP400, where the lowest amount of ash was found when applying a 10 K/min heating rate. However, in this case, the differences could have been due to higher heterogeneity in the sample.

As previously mentioned, TGA allows definition of the temperature at which maximum weight loss is produced (T_p) and also the temperature at which the reaction accelerates (IT). Those values are reported in Table 5. Note that the IT and T_p values for the two olive samples in Table 5 have been previously reported by Castells et al. [34].

Table 5. TGA parameters results.

Sample	T_p 5 K/min	T_p 10 K/min	T_p 20 K/min	IT 5 K/min	IT 10 K/min	IT 20 K/min
OPI	276.7	294.4	335.1	240.8	255.2	257.7
OCP	295.6	296.9	303.5	208.6	230.1	242.7
POP	333.1	342.3	344.5	270.0	282.2	288.0
PP400	346.5	344.6	357.3	294.0	293.5	309.0
PP250	347.5	352.2	356.2	294.0	299.2	309.0
PP80	347.4	354.2	355.3	291.3	296.3	303.0

From the results reported in Table 5 and Figures S1–S6, it can be deduced that the higher the heating rate applied, the higher the IT and T_p values, since the TGA curve shifted slightly to the right, as has previously been pointed out by other authors [87]. When the heating rate is increased, the area under the DTG curve enlarges and the shape becomes smooth [88]. A higher heating rate produces a thermal lag, as the sample does not

have the time required to properly reach the specific temperature, so some processes are smoothed and the stages cannot be differentiated, leading to higher *IT* and T_p values. This fact is illustrated in Figures S1–S6 for each material. For example, all the samples in the 5 K/min DTG curves presented a left shoulder due to hemicellulose decomposition [89], and the OPI sample, in which the polymers were more clearly differentiated, produced two obvious peak curves. However, when the heating rate was increased, this shoulder disappeared, as hemicellulose decomposition took place at the same time as the other polymers degraded [90].

When assessing PP400, PP250 and PP80 samples, it is clear that they behaved very similarly as they were the same material. As a consequence, only slight differences in the reported values can be appreciated. Nevertheless, these differences might lead to dissimilar kinetic values. On the other hand, Table 1 shows that the olive samples presented lower *IT* and T_p temperatures than the woody samples, which means that the combustion of olive residues accelerated and achieved the maximum rate sooner than the woody materials did.

As illustrated in Figures S1–S6, the hemicellulose peak was clearer in the olive samples than in the woody samples (particularly in the OPI curve). Indeed, the combustion of olive residues seemed to be composed of different degradation stages, since the curves showed changes of slope. This behaviour can be seen more clearly in the OCP curve, where the clear right shoulder is linked to lignin degradation [91].

3.2. Fraser–Suzuki Composition Model Results

As previously explained, the Fraser–Suzuki deconvolution was applied using $n = 3$ to estimate the hemicellulose, cellulose and lignin contents. Hemicellulose is the first polymer to degrade in a range of temperatures between 200 °C and 320 °C, followed by cellulose, whose devolatilisation temperature range is between 300 °C and 400 °C. Finally, lignin is the most stable polymer, and its full degradation requires a wider temperature range of between 200 °C and 800 °C [92]. Considering these ranges of temperature, pseudocomponent 1 (PS1) was assigned to hemicellulose, pseudocomponent 2 (PS2) to cellulose and pseudocomponent 3 (PS3) to lignin. The results for each polymer together with the R^2 fitting parameter are shown in Table 6, while Figures S7–S12 show the fitting and the area that relate to each polymer content.

Table 6. Fraser–Suzuki deconvolution results.

Sample	PS1 (%)	PS2 (%)	PS3 (%)	R^2
OPI	27.6	15.6	56.9	0.9964
OCP	14.3	34.5	51.2	0.9744
POP	26.0	46.4	27.6	0.9876
PP400	36.8	39.0	24.2	0.9615
PP250	21.7	49.2	29.2	0.9723
PP80	24.2	47.0	28.8	0.9774

Again, the differences between the olive and woody samples were obvious. When considering the three pine wood curves, the distributions were very similar, which is consistent as they were the same material; the same composition was expected. It must be noted that PP400 showed slightly different values to PP250 and PP80. This difference could have been due to the deconvolution process itself, as has previously been noted by other authors [93]; PP400 gave the lowest R^2, which means that the fitting method might not be accurate enough and therefore induces small errors.

Nevertheless, the results indicate that the main component was cellulose in all the woody samples, with values between 39% and 49%, followed by lignin and hemicellulose; sample PP400 presented more hemicellulose than lignin. If compared to previous data in the literature (using both theoretical estimations and chemical analysis), a wide range of values can be found. However, they all show the same trend, which is consistent with the results obtained in this study [94–97]. For example, when comparing the results with the

data reported by Shang et al. [96], the lignin content for pine pellets presented in this study was slightly lower. However, other authors have shown that lignin content also depends on pine type, showing differences between *Pinus sylvestris* and *Pinus pinea* [94]. If the lignin content is compared to that for Scots pine pellets by Zborowska et al. [97], the values presented here are consistent, and so is the cellulose, which is the predominant polymer.

The estimated composition of the POP sample was similar to that of the pine pellets, as both are woody biomass materials. Again, the results were consistent with the previously published literature, showing a high content of cellulose, followed by hemicellulose and, finally, a small percentage of lignin [98,99].

On the other hand, the olive samples presented a significantly high content of lignin. This fact can be explained by the type of sample, as lignin is the main structural component of shells and stones that binds cellulose and hemicellulose [100]. Figures S7–S12 illustrate that lignin decomposed over a wide range of temperatures on the two olive curves and also presented a large area below that led to amounts greater than 50%. This significant content is the reason that olive waste can be used for extracting lignin [101–104].

3.3. Combustion Indices Results

For each sample and heating rate, the combustion indices were calculated. The results are presented in Table 7 together with the average values.

Table 7. Combustion indices obtained for each of the three heating rates and mean values.

Sample	β (K/min)	D_i (%/min^3)	D_b (%/min^4)	S (%^{2}/min^2 × °C^3)	H_f (°C × min^2/%)	C (%/min × °C^2)	D_w (%/min × °C^2)
OPI	5	1.42×10^{-3}	2.11×10^{-5}	7.52×10^{-8}	1168.84	4.81×10^{-5}	4.24×10^{-5}
	10	9.10×10^{-3}	2.95×10^{-4}	2.08×10^{-7}	888.59	7.66×10^{-5}	6.85×10^{-5}
	20	5.33×10^{-2}	3.54×10^{-3}	5.10×10^{-7}	607.93	1.18×10^{-4}	1.06×10^{-4}
	Mean	2.13×10^{-2}	1.29×10^{-3}	2.64×10^{-7}	888.45	8.09×10^{-5}	7.22×10^{-5}
OCP	5	1.01×10^{-3}	2.38×10^{-5}	7.39×10^{-8}	1210.06	4.23×10^{-5}	3.03×10^{-5}
	10	7.39×10^{-3}	2.86×10^{-4}	1.87×10^{-7}	906.80	7.97×10^{-5}	6.30×10^{-5}
	20	3.69×10^{-2}	3.61×10^{-3}	5.85×10^{-7}	544.96	1.34×10^{-4}	1.06×10^{-4}
	Mean	1.51×10^{-2}	1.31×10^{-3}	2.82×10^{-7}	887.27	8.53×10^{-5}	6.63×10^{-5}
POP	5	1.41×10^{-3}	2.72×10^{-5}	8.73×10^{-8}	1405.66	4.87×10^{-5}	4.01×10^{-5}
	10	9.88×10^{-3}	3.60×10^{-4}	2.31×10^{-7}	1093.42	8.85×10^{-5}	7.36×10^{-5}
	20	6.19×10^{-2}	4.34×10^{-3}	6.78×10^{-7}	639.70	1.45×10^{-4}	1.23×10^{-4}
	Mean	2.44×10^{-2}	1.57×10^{-3}	3.32×10^{-7}	1046.26	9.39×10^{-5}	7.89×10^{-5}
PP400	5	1.50×10^{-3}	2.59×10^{-5}	8.88×10^{-8}	1501.37	5.01×10^{-5}	4.31×10^{-5}
	10	1.05×10^{-2}	3.58×10^{-4}	2.70×10^{-7}	1045.52	8.71×10^{-5}	7.54×10^{-5}
	20	6.04×10^{-2}	4.31×10^{-3}	5.70×10^{-7}	678.95	1.26×10^{-4}	1.11×10^{-4}
	Mean	2.41×10^{-2}	1.56×10^{-3}	3.10×10^{-7}	1075.28	8.76×10^{-5}	7.65×10^{-5}
PP250	5	1.54×10^{-3}	2.68×10^{-5}	8.68×10^{-8}	1515.35	4.97×10^{-5}	4.24×10^{-5}
	10	9.51×10^{-3}	3.25×10^{-4}	2.21×10^{-7}	1116.27	8.16×10^{-5}	7.10×10^{-5}
	20	6.52×10^{-2}	4.55×10^{-3}	5.75×10^{-7}	690.00	1.26×10^{-4}	1.11×10^{-4}
	Mean	2.54×10^{-2}	1.63×10^{-3}	2.94×10^{-7}	1107.20	8.57×10^{-5}	7.48×10^{-5}
PP80	5	1.37×10^{-3}	2.42×10^{-5}	7.45×10^{-8}	1588.78	5.30×10^{-5}	4.47×10^{-5}
	10	8.97×10^{-3}	3.15×10^{-4}	2.12×10^{-7}	1136.85	8.17×10^{-5}	6.92×10^{-5}
	20	6.25×10^{-2}	4.52×10^{-3}	6.01×10^{-7}	655.65	1.31×10^{-4}	1.16×10^{-4}
	Mean	2.43×10^{-2}	1.62×10^{-3}	2.96×10^{-7}	1127.09	8.85×10^{-5}	7.68×10^{-5}

Analysis of these results demonstrated that the increase in heating rate during TGA led to a growth in all parameters except for the combustion intensity index (H_f), which notably decreased; these results agreed with those reported by Xu et al. for pine wood [46].

The PP250 and PP80 samples showed remarkably high values for both the ignition (D_i) and combustion (D_b) indices. These results suggest that these samples have a higher ignition

ease and combustion efficiency, particularly under higher heating rates. This fact might be related to the smaller particle size of these samples, which would increase the surface area and promote heat and mass transfer during combustion. These findings are in line with those reported in the literature for wood and olive residue samples [46,105]. In addition, it is important to note that the POP and PP400 samples exhibited the greatest comprehensive combustion index (S) at the highest heating rate, so these samples could achieve a better overall combustion performance. The high values of these samples indicate that not only did they ignite easily but also an efficient combustion was maintained throughout the process.

When comparing the ignition index (D_i) with the HHV reported in Table 1, it was noted that the two parameters followed similar trends. Although all samples presented similar high heating values, PP and OPI showed the greatest HHV, while OCP had the lowest; this agreed quite well with the D_i values. Indeed, D_i is related to volatile release efficiency during combustion. However, not all the indices in Table 7 showed clear correlation with the HHV values. As mentioned earlier, the differences in HHV were very small, while the combustion indices could give further information about the performance of each sample.

Samples POP, PP80 and PP400 showed the highest values of the flammability index (C), indicating that they tend to have better combustibility and higher ignition stability. In contrast, the PP250, OPI and OCP samples showed lower stability, suggesting lower fire spread at higher temperatures.

If the integral combustion (S) and flammability (C) indices are compared with the literature, it can be said that the S values of pine wood obtained in the present study are close and the C values are lower to those reported by Xu et al. [46]. On the other hand, the values for the olive residue samples were similar to those reported by Wzorek et al. [105].

In addition, a comparison of the indices listed above with those reported in [106] for heating rates from 10 to 100 K/min detected that they were all very close. Regarding the combustion intensity index (H_f) of the pine samples (PP400, PP250 and PP80), it was observed that smaller particle size corresponded to a higher value of this parameter, especially at lower heating rates. This trend was consistent for all heating rates except for PP80 at 20 K/min, where a slight deviation was observed. On the other hand, the value for OPI was the lowest and OCP the highest, which means OCP presented the less efficient combustion process.

Concerning the combustion stability index (D_w), it can be seen that the samples followed a similar pattern to the case of the flammability index (C). The POP, PP80, and PP400 samples gave the highest values, indicating that they have greater stability during the combustion process. Comparing D_w with previous data in the literature, it was observed that the results were slightly lower than those reported for wood samples by Bilkic et al. [73], while there are no previous data for olive residues.

The thermal behaviour of biomass samples revealed the crucial role of the heating rate. A significant increase in the values of D_i, D_b, C and D_w was observed with a growth in the heating rate, indicating a greater propensity for sample ignition. Conversely, the opposite was noted for H_f: Their values decreased with higher heating rates, meaning lower energy was involved.

3.4. Kinetic Analysis Results

The results obtained from the kinetic analysis are illustrated in Figures S13–S18 in the Supplementary Materials, where results are plotted for each sample and method. The curves represent the evolution of activation energy in terms of the conversion factor. Figures S19–S21 show the pre-exponential factor evolution with the conversion, while Figures S22–S30 illustrate the activation energy values of the different models, along with error bars corresponding to the mathematical modelling (upper and lower 95% prediction bounds). The values obtained at the end of the curves represent char formation, while the devolatilisation process comprised between 0.2 and 0.6, approximately.

The woody samples presented similar behaviours and trends, whereas again the olive waste samples gave different results. The woody samples had quite stable *Ea* values in the range of 0.2 and 0.6, except for PP8, followed by a drastic drop between 0.6 and 0.7. The curves show that, as the temperature increased after a certain level, *Ea* decreased; this can be explained by particle collision [107]. After that point, *Ea* increased again. Some authors have already noted this behaviour in woody samples, even a heavy increase for $\alpha \geq 0.8$ [108]. In contrast, the olive samples consistently increased their activation energy, producing a peak around α = 0.6–0.7, with *Ea* then dropping at the end of the conversion. Nevertheless, it is clear that the main devolatilisation process took place between 0.2 and 0.6, where the activation energy varied less [109,110].

The average activation energy and pre-exponential values for each sample and method are reported in Table 8 (note that the results for OPI and OCP have been reported by Castells et al. [34]).

Table 8. Friedman, KAS and FWO mean kinetic results.

Sample	Friedman		KAS		FWO	
	Ea **(kJ/mol)**	***A*** **(s^{-1})**	***Ea*** **(kJ/mol)**	***A*** **(s^{-1})**	***Ea*** **(kJ/mol)**	**A (s^{-1})**
OPI	128.58	4.12×10^{42}	154.73	1.14×10^{44}	156.56	3.35×10^{42}
OCP	294.19	2.10×10^{44}	251.72	6.60×10^{45}	248.17	1.69×10^{44}
POP	157.66	1.58×10^{41}	191.76	3.94×10^{42}	191.86	1.29×10^{41}
PP400	174.59	3.01×10^{40}	204.44	7.12×10^{41}	203.93	2.47×10^{40}
PP250	162.90	1.25×10^{40}	187.19	2.86×10^{41}	187.66	1.02×10^{40}
PP80	94.10	1.26×10^{40}	118.07	2.89×10^{41}	121.89	1.03×10^{40}

OPI showed significantly lower values than OCP but both materials showed consistent results compared to the literature [33,111]. Regarding the poplar sawdust, the results when using KAS and FWO were slightly higher than the reported values, which are usually between 130 and 170 kJ/mol [112–114], but aligned with the literature if the Friedman method was considered. However, *Ea* values in the literature for woody samples present significant variability. Indeed, values between 130 and 205 kJ/mol have been reported for pine samples [46,115,116], a range within which the results for PP400 and PP250 fell. On the other hand, PP80 showed lower activation energies due to its particle size [117].

If the differences between the methods are considered, it can be seen that Friedman provided slightly different values to KAS and FWO. The reason is that KAS and FWO are derived from the same mathematical model, while Friedman might lead to numeral instability when applying conversion rate data [76]. As Friedman is a differential method, the results are more sensitive to instantaneous changes in reaction kinetics. On the other hand, KAS and FWO are integral methods, so they average kinetic behaviour and, in some cases, underestimate activation energy. These differences are reflected in changes in the reaction mechanism. Comparing the kinetic parameters of the samples in Table 8, the same trends were obtained following the three methods except for the OCP sample; KAS and FWO gave smaller *Ea* values than Friedman for OCP, whereas the contrary was true for the rest of samples. Overall, KAS and FWO seem to provide more accurate results, as no assumption regarding the mechanism is made.

The pre-exponential factors obtained in this study were higher than the values reported in the previously published literature. However, Rego et al. [118] explained that, when employing a model-free kinetics approach, a mathematical relationship exists between the pre-exponential factor and activation energy. Since activation energy changes in accordance with the extent of pyrolysis, the pre-exponential factor also undergoes similar variations.

The olive samples also presented similar values for KAS and FWO methods and differed for Friedman. These samples showed the greatest pre-exponential factor values. As can be seen in Figures S13–S18, the highest peak of *Ea* was produced close to 0.6, when the hemicellulose and cellulose had already been devolatilised, and activation energy then

increased due to the stability of lignin, which required higher activation energies to break the chemical chains and properly initiate the reaction. Indeed, most samples showed a peak around α~0.6, particularly OPI, which recorded the highest activation energy peak; OPI also presented the highest lignin content (see Table 6). Nevertheless, despite having a higher *Ea* peak, OPI registered a lower average *Ea* value than OCP. This was probably due to cellulose content: OCP had more cellulose, which degrades at higher temperatures than hemicellulose, and it could have led to a more stable *Ea* curve as the degradation process was prolonged. Moreover, OCP is the only sample that showed an increase in activation energy between α~0.6–0.7. This could be explained by the composition of the sample, since OCP presented the greatest amount of residue (~30%) due to the presence of inorganic compounds [119]; as can be seen in Table 2, OCP had the highest ash content. This fact, together with the important lignin content of the sample, led to an increase of activation energy at the end of the conversion [120].

Regarding the woody samples, no significant difference was found between poplar sawdust (POP) and pine pellets. Indeed, the reported values for both samples—between 150 and 205 kJ/mol—are consistent with the previously published literature, although the average activation energies were a little higher than in previous studies [31,121]. Nevertheless, Anca-Couce et al. [44] have already highlighted a wide range of activation energies when comparing data from different studies, since the results depend on several parameters such as kinetic model implementation and TGA procedure.

Regarding the shape of the PP400 and PP250 curves, again, the significant amount of cellulose led to a stable *Ea* curve, in contrast to PP80. Indeed, significant differences were detected between samples of wood pellets with different particle size. The *Ea* values in Table 8 reduced when the particle size decreased, as the transfer mechanisms are more efficient, leading to an increase in the reaction order and a decrease in activation energy and pre-exponential factor [109].

In most of the samples it was noted that between $\alpha = 0.6$ and $\alpha = 0.7$ the activation energy curves behave differently, leading to modifications in the *Ea* trend. Similar behaviour has been previously observed by other authors, and this fact can be explained by the multiple overlapping reactions that take place at this point of the conversion [122,123]. This complexity affects the linearity of the models and produces alterations in the activation energy values. After mid-conversion, not only does the devolatilisation of lignin take place but so also does char formation and volatile release [36,124].

Significant correlations between the activation energy (*Ea*) and combustion indices were detected. An inverse relationship between *Ea* and the ignition index (D_i) was observed, particularly for the OCP sample, which presented the highest *Ea* and the lowest D_i (1.51×10^{-2}%/min^3). This trend was also detected in the pine samples, where PP80 and PP250, with lower *Ea* values than PP400, showed higher D_i. Therefore, it seems that materials with lower *Ea* tend to have higher ignition indices; this indicates easier combustion due to a high volatile content. Combustion stability, quantified by the flammability (C) and stability (D_w) indices, showed a correlation with the variation of *Ea* throughout the conversion range. The wood samples, especially POP, exhibited more stable *Ea* curves and higher values of C (9.39×10^{-5}%/min×°C^2) and D_w (7.89×10^{-5}%/min×°C^2) than the olive samples. OCP, having the worst H_f value and the highest *Ea*, emphasises the relationship between activation energy and combustion efficiency.

3.5. Thermodynamic Parameters Results

The results obtained from the thermodynamic analysis are presented in Figures S31–S39 of the Supplementary Materials, where ΔH, ΔH vs. *Ea*, ΔG and ΔS curves are plotted for each conversion grade considering the three kinetic models. The average values are reported in Figures 1–3. In addition, Figure 4 compares the enthalpy and the activation energy for each sample. (Note that the curves for KAS and FWO overlapped.)

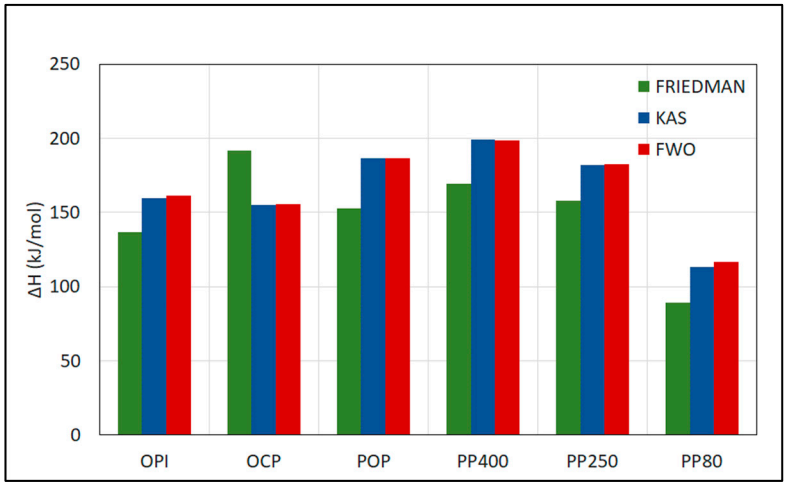

Figure 1. Δ*H* results for each sample and method.

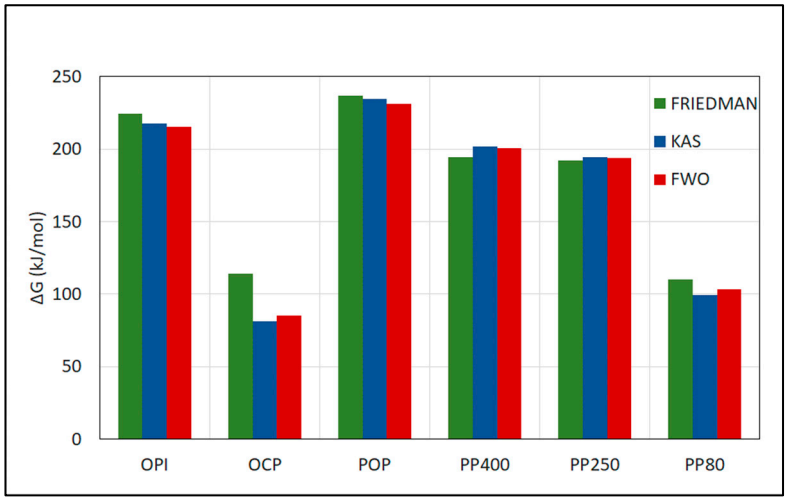

Figure 2. Δ*G* results for each sample and method.

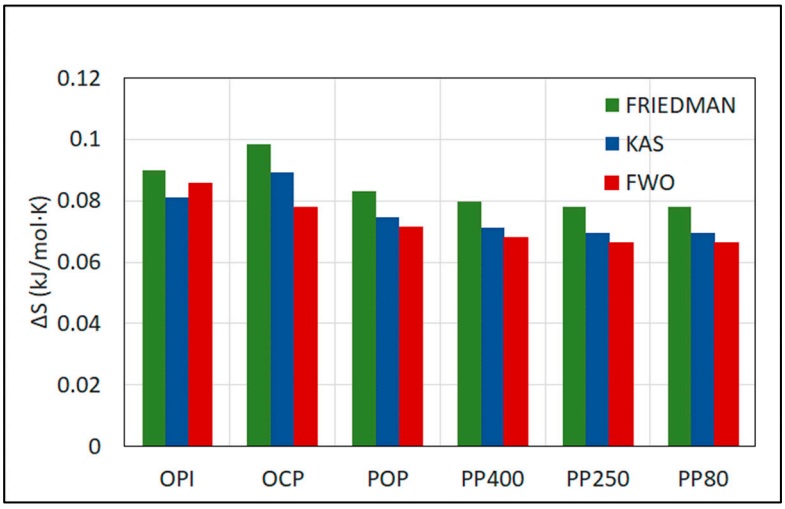

Figure 3. Δ*S* results for each sample and method.

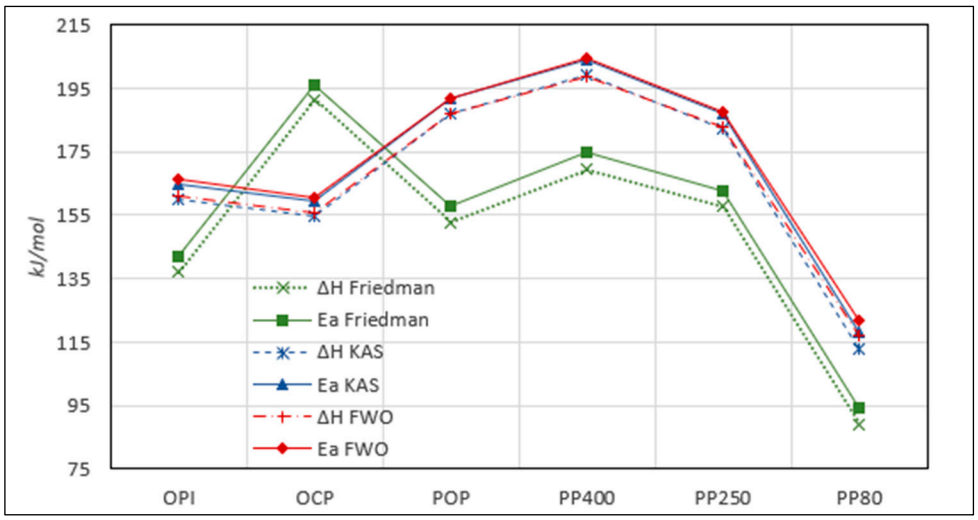

Figure 4. Comparison of Δ*H* to *Ea* results for each sample following the three kinetic methods.

Δ*H* represents the difference in energy between the reactants and products. As can be seen in Figure 1, OPI showed Δ*H* values between 137.02 and 161.2 kJ/mol, while OCP presented a wider range, from 154.93 to 191.47 kJ/mol. These values are very close to those obtained by Sánchez-Ávila et al. [125], who reported 185 kJ/mol for olive residue samples. POP gave values between 152.66 and 186.85 kJ/mol, which are close to 169.46 kJ/mol by Sharma et al. [113]. On the other hand, samples PP400, PP250 and PP80 showed a clear declining trend when particle size decreased, regardless of the method; for example, from 198.78 kJ/mol for PP400 to 116.82 kJ/mol for PP80 when using FWO. These figures are close to other values reported in the literature [46]. This trend implies a higher susceptibility to ignition in the case of small particles, since they require less activation energy. Therefore, they are more prone to spontaneous ignition. In addition, the risk of explosion also increases as the easier decomposition of these fine particles can lead to faster flame propagation and a more severe explosion.

Due to the dependence between enthalpy and activation energy, the variations of Δ*H* with α in Figure 1 were quite similar to those of *Ea* in Figure 4, suggesting that the feasibility of the reactions occurring in the combustion of the samples varied with α. The values obtained in this study were similar to those reported in the literature, except for those of the PP80 sample, which were lower [26].

The small difference between *Ea* and Δ*H*, which was approximately ±5 kJ/mol according to Figure 4, reveals the viability of the reaction. A smaller gap between *Ea* and Δ*H* implies a greater preference for product formation [76], i.e., a more complete combustion. Figure 4 also illustrates that OCP is the only sample that presented different behaviour when the three kinetic models were compared. The Friedman activation energy and the corresponding enthalpy of OCP were greater than the values obtained when using KAS or FWO. The opposite was true for the rest of samples.

Gibbs free energy (Δ*G*) quantifies the energy available from biomass combustion. Elevated Δ*G* values indicate a higher degree of difficulty for corresponding thermal degradation and vice versa. The Δ*G* values obtained in the present analysis ranged from 81.3 to 236.8 kJ/mol, as illustrated in Figure 2. These values were found to be similar to data reported in the literature [112,126]. As for Δ*H*, a decrease in Gibbs free energy was observed when particle size decreased. This trend has safety implications: smaller particles present higher reactivity because they require less energy to reach the transition state, as well as shorter induction time and faster propagation. Moreover, with the development of combustion, the favourability of the reactions remained almost constant throughout the process, particularly in the case of the KAS and FWO methods [26].

Δ*S* quantifies the randomness or disorder of energy and matter within the system. As shown in Figures S37–S39 of the Supplementary Materials, the Δ*S* values for the different

conversion degrees (α) were positive, indicating that the level of disorder in the combustion reaction products was higher than that in the reactants. Positive values of both ΔG and ΔS suggest that the thermal decomposition of the samples is a non-spontaneous process, and that there is high energy dispersion in the system.

OPI and OCP presented entropy values higher than those reported by Sánchez-Ávila et al. [125]. In this study, OPI showed values between 0.081 and 0.090 kJ/mol×K, while OCP gave values between 0.078 and 0.098 kJ/mol×K. On the other hand, POP had values between 0.071 and 0.083 kJ/mol×K, which are lower than those reported for olive residues. Regarding samples PP400, PP250 and PP80, the same trend reported above was observed; ΔS decreased for smaller particle sizes (from 0.080 kJ/mol×K to 0.078 kJ/mol×K for Friedman).

The thermodynamic parameters presented some trends that were consistent with the results presented in previous sections. For example, wood samples POP, PP400 and PP250 had higher ΔH—if the KAS or FWO methods were followed—and showed more favourable combustion indices than the olive samples. For instance, POP gave higher C (9.39×10^{-5}%/min×°C^2) and D_w (7.89×10^{-5}%/min×°C^2) values than the olive samples. The burnout index (D_b) showed a positive correlation with enthalpy values for most samples, except for the PP80 sample. The pine sample PP80 had a low ΔG and a relatively high D_i (2.43×10^{-2}%/min^3), which could suggest a higher tendency to spontaneous processes.

4. Conclusions

This study aimed to characterise the combustion process of olive residues and woody samples using TGA data and isoconversional methods to calculate kinetic parameters, the Fraser–Suzuki deconvolution technique to estimate biomass composition, and a set of indices to evaluate combustion behaviour.

Although the TGA showed the same stages for every sample, significant differences were found between the two groups of biomass samples considered in this study. The lignin content present in the olive pits and olive cake was found to be significantly higher than the content in the woody samples.

Apart from the composition, thermal behaviour was also found to be different, which of course led to some variation in the combustion, thermodynamic and kinetic parameters. Furthermore, differences were found not only between types of biomass but also between samples with different particle size of the same material (wood pellets). Due to the small crucibles used in the TGA tests, research usually focuses on the type of biomass, neglecting particle size effects. However, this study has proven that particle size has an influence on the results. The lower the particle size, the more efficient the combustion was, since the heat transfer mechanisms were more optimal, leading to lower activation energy, pre-exponential factor, enthalpy and free Gibbs energy. In addition, the heating rate applied during TGA affected the combustion indices.

The kinetic analysis has proven to be stable, as the values for every kinetic model led to almost constant values, which were consistent with the previously published literature. KAS and FWO gave similar values, as they use the same mathematical model, whereas the results obtained following the Friedman method deviated from the KAS and FWO results.

It is important to note the usefulness of defining the thermodynamic parameters, which could provide a better characterisation of the sample energy conversion process. Indeed, the variations in enthalpy, entropy and Gibbs free energy exposed the non-spontaneity of the reactions, as well as high dispersion in the system. Furthermore, the low difference between the activation energy (Ea) and enthalpy (ΔH) revealed the viability of the reactions.

Moreover, the relationships found between the combustion indices and the kinetic and thermodynamic parameters must be highlighted. The ignition index showed an inverse relationship with the activation energy, while the burnout index correlated with the enthalpy for most samples. Combustion stability indices were related to the uniformity of the Ea curves throughout the conversion range. The combustion intensity index exhibited an inverse correlation with Gibbs free energy.

Further studies could consider applying the Fraser–Suzuki deconvolution to a distributed activation energy model (DAEM) to analyse the influence of each component in the activation energy of the sample. Furthermore, the determination of not only the kinetic parameters but also the thermodynamic parameters and combustion indices of cellulose, hemicellulose and lignin could help to contrast and compare different conversion methods.

Supplementary Materials: The following supporting information can be downloaded at https://www.mdpi.com/article/10.3390/fire7110396/s1, Figure S1: TGA (solid lines) and DTG (dotted lines) curves for OPI and three heating rates; Figure S2: TGA (solid lines) and DTG (dotted lines) curves for OCP and three heating rates; Figure S3: TGA (solid lines) and DTG (dotted lines) curves for POP and three heating rates; Figure S4: TGA (solid lines) and DTG (dotted lines) curves for PP400 and three heating rates; Figure S5: TGA (solid lines) and DTG (dotted lines) curves for PP250 and three heating rates; Figure S6: TGA (solid lines) and DTG (dotted lines) curves for PP80 and three heating rates; Figure S7: OPI Fraser-Suzuki deconvolution curves; Figure S8: OCP Fraser-Suzuki deconvolution curves; Figure S9: POP Fraser-Suzuki deconvolution curves; Figure S10: PP400 Fraser-Suzuki deconvolution curves; Figure S11: OPI Fraser-Suzuki deconvolution curves; Figure S12: PP80 Fraser-Suzuki deconvolution curves; Figure S13: OPI kinetic results for each method; Figure S14: OCP kinetic results for each method; Figure S15: POP kinetic results for each method; Figure S16: PP400 kinetic results for each method; Figure S17: PP250 kinetic results for each method; Figure S18: PP80 kinetic results for each method; Figure S19: Preexponential factor calculated according to Friedman method (right *y*-axis represents OCP); Figure S20: Preexponential factor calculated according to KAS method (right *y*-axis represents OCP); Figure S21: Preexponential factor calculated according to FWO method (right *y*-axis represents OCP); Figure S22: Activation energy calculated according to Friedman method; Figure S23: Activation energy calculated according to KAS method; Figure S24: Activation energy calculated according to FWO method; Figure S25: OPI Activation energy values with confidence intervals; Figure S26: OCP Activation energy values with confidence intervals; Figure S27: POP Activation energy values with confidence intervals; Figure S28: PP400 Activation energy values with confidence intervals; Figure S29: PP250 Activation energy values with confidence intervals; Figure S30: PP80 Activation energy values with confidence intervals; Figure S31: Enthalpy variation versus conversion factor, calculated according to Friedman method; Figure S32: Enthalpy variation versus conversion factor, calculated according to KAS method; Figure S33: Enthalpy variation versus conversion factor, calculated according to FWO method; Figure S34: Gibbs free energy variation versus conversion factor, calculated according to Friedman method; Figure S35: Gibbs free energy variation versus conversion factor, calculated according to KAS method; Figure S36: Gibbs free energy variation versus conversion factor, calculated according to FWO method; Figure S37: Entropy variation versus conversion factor, calculated according to Friedman method; Figure S38: Entropy variation versus conversion factor, calculated according to KAS method; Figure S39: Entropy variation versus conversion factor, calculated according to FWO method.

Author Contributions: Conceptualisation, R.P. and B.C.; methodology, R.P. and B.C.; formal analysis, R.P. and B.C.; investigation, R.P. and B.C.; resources, B.C. and A.T.; writing—original draft preparation, R.P. and B.C.; writing—review and editing, B.C. and A.T.; visualisation, R.P. and B.C.; project administration, B.C. and A.T. All authors have read and agreed to the published version of the manuscript.

Funding: This research was partly funded by the Autonomous Community of La Rioja (Gobierno de La Rioja) through grant No. PID2019-106560RA-I00.

Institutional Review Board Statement: Not applicable.

Informed Consent Statement: Not applicable.

Data Availability Statement: The original contributions presented in the study are included in the article/supplementary material, further inquiries can be directed to the corresponding author/s.

Conflicts of Interest: The authors declare no conflicts of interest.

References

1. Neves, S.A.; Marques, A.C.; Patrício, M. Determinants of CO_2 emissions in European Union countries: Does environmental regulation reduce environmental pollution? *Econ. Anal. Policy* **2020**, *68*, 114–125. [CrossRef]
2. European Commission. The Paris Protocol—A blueprint for tackling change beyond 2020. *Communication* **2015**, *17*, 1–17.
3. Scarlat, N.; Dallemand, J.-F.; Monforti-Ferrario, F.; Banja, M.; Motola, V. Renewable energy policy framework and bioenergy contribution in the European Union—An overview from National Renewable Energy Action Plans and Progress Reports. *Renew. Sustain. Energy Rev.* **2015**, *51*, 969–985. [CrossRef]
4. Solano Rodriguez, B.; Drummond, P.; Ekins, P. Decarbonizing the EU energy system by 2050: An important role for BECCS. *Clim. Policy* **2017**, *17*, S93–S110. [CrossRef]
5. Vakulchuk, R.; Overland, I.; Scholten, D. Renewable energy and geopolitics: A review. *Renew. Sustain. Energy Rev.* **2020**, *122*, 109547. [CrossRef]
6. Farrell, A.E.; Gopal, A.R. Bioenergy Research Needs for Heat, Electricity, and Liquid Fuels. *MRS Bull.* **2008**, *33*, 373–380. [CrossRef]
7. Srivastava, R.K.; Shetti, N.P.; Reddy, K.R.; Kwon, E.E.; Nadagouda, M.N.; Aminabhavi, T.M. Biomass utilization and production of biofuels from carbon neutral materials. *Environ. Pollut.* **2021**, *276*, 116731. [CrossRef]
8. Schlamadinger, B.; Apps, M.; Bohlin, F.; Gustavsson, L.; Jungmeier, G.; Marland, G.; Pingoud, K.; Savolainen, I. Towards a standard methodology for greenhouse gas balances of bioenergy systems in comparison with fossil energy systems. *Biomass Bioenergy* **1997**, *13*, 359–375. [CrossRef]
9. Christoforou, E.; Fokaides, P.A. Sustainability Considerations of Solid Biofuels Production and Exploitation. In *Advances in Solid Biofuels: Green Energy and Technology*; Springer: Cham, Switzerland, 2019; pp. 97–109.
10. McKendry, P. Energy production from biomass (part 2): Conversion technologies. *Bioresour. Technol.* **2002**, *83*, 47–54. [CrossRef]
11. Bilgili, F.; Koçak, E.; Bulut, Ü.; Kuşkaya, S. Can biomass energy be an efficient policy tool for sustainable development? *Renew. Sustain. Energy Rev.* **2017**, *71*, 830–845. [CrossRef]
12. Nikolaisen, L.S.; Jensen, P.D. Biomass feedstocks: Categorisation and preparation for combustion and gasification. In *Biomass Combustion Science, Technology and Engineering*; Elsevier: Amsterdam, The Netherlands, 2013; pp. 36–57.
13. Osman, A.I.; Mehta, N.; Elgarahy, A.M.; Al-Hinai, A.; Al-Muhtaseb, A.H.; Rooney, D.W. Conversion of biomass to biofuels and life cycle assessment: A review. *Environ. Chem. Lett.* **2021**, *19*, 4075–4118. [CrossRef]
14. Tursi, A. A review on biomass: Importance, chemistry, classification, and conversion. *Biofuel Res. J.* **2019**, *6*, 962–979. [CrossRef]
15. Hongzhang, C. *Lignocellulose Biorefinery Engineering*; Woodhead Publishing Limited: Cambridge, UK, 2015.
16. Fernandez-Lopez, M.; Pedrosa-Castro, G.J.; Valverde, J.L.; Sanchez-Silva, L. Kinetic analysis of manure pyrolysis and combustion processes. *Waste Manag.* **2016**, *58*, 230–240. [CrossRef] [PubMed]
17. Vassilev, S.V.; Baxter, D.; Andersen, L.K.; Vassileva, C.G. An overview of the composition and application of biomass ash. *Fuel* **2013**, *105*, 19–39. [CrossRef]
18. Achinas, S.; Achinas, V.; Euverink, G.J.W. A Technological Overview of Biogas Production from Biowaste. *Engineering* **2017**, *3*, 299–307. [CrossRef]
19. Ilic, D.; Williams, K.; Farnish, R.; Webb, E.; Liu, G. On the challenges facing the handling of solid biomass feedstocks. *Biofuels Bioprod. Biorefin.* **2018**, *12*, 187–202. [CrossRef]
20. Castells, B.; Amez, I.; Medic, L.; García Torrent, J. Particle Size Influence on the Transport Classification Labels and Other Flammability Characteristics of Powders. *Appl. Sci.* **2020**, *10*, 8601. [CrossRef]
21. Varela, A.; Arbizu-Milagro, J.; Tascón, A. Application of Factorial Analysis to the Study of Vented Dust Explosions in Large Biomass Storage Silos. *Fire* **2023**, *6*, 226. [CrossRef]
22. Babiński, P.; Łabojko, G.; Kotyczka-Morańska, M.; Plis, A. Kinetics of coal and char oxycombustion studied by TG–FTIR. *J. Therm. Anal. Calorim.* **2013**, *113*, 371–378. [CrossRef]
23. Vyazovkin, S.; Burnham, A.K.; Criado, J.M.; Pérez-Maqueda, L.A.; Popescu, C.; Sbirrazzuoli, N. ICTAC Kinetics Committee recommendations for performing kinetic computations on thermal analysis data. *Thermochim. Acta* **2011**, *520*, 1–19. [CrossRef]
24. Álvarez, A.; Pizarro, C.; García, R.; Bueno, J.; Lavín, A. Determination of kinetic parameters for biomass combustion. *Bioresour. Technol.* **2016**, *216*, 36–43. [CrossRef] [PubMed]
25. Ashraf, A.; Sattar, H.; Munir, S. A comparative applicability study of model-fitting and model-free kinetic analysis approaches to non-isothermal pyrolysis of coal and agricultural residues. *Fuel* **2019**, *240*, 326–333. [CrossRef]
26. Chen, R.; Li, Q.; Xu, X.; Zhang, D.; Hao, R. Combustion characteristics, kinetics and thermodynamics of Pinus Sylvestris pine needle via non-isothermal thermogravimetry coupled with model-free and model-fitting methods. *Case Stud. Therm. Eng.* **2020**, *22*, 100756. [CrossRef]
27. Gao, M.; Pan, D.X.; Sun, C.Y. Study on the thermal degradation of wood treated with amino resin and amino resin modified with phosphoric acid. *J Fire Sci* **2003**, *21*, 189–201. [CrossRef]
28. Deka, M.; Saikia, C.N.; Baruah, K.K. Studies on thermal degradation and termite resistant properties of chemically modified wood. *Bioresour. Technol.* **2002**, *84*, 151–157. [CrossRef]
29. Zakrzewski, R. Pyrolysis kinetics of wood comparison of iso and polythermal thermogravimetric methods. *Electron. J. Pol. Agric. Univ.* **2003**, *6*.
30. Yorulmaz, S.Y.; Atimtay, A.T. Investigation of combustion kinetics of treated and untreated waste wood samples with thermogravimetric analysis. *Fuel Process. Technol.* **2009**, *90*, 939–946. [CrossRef]

31. Gašparovič, L.; Koreňová, Z.; Jelemenský, Ľ. Kinetic study of wood chips decomposition by TGA. *Chem. Pap.* **2010**, *64*, 174–181. [CrossRef]
32. Sfakiotakis, S.; Vamvuka, D. Study of co-pyrolysis of olive kernel with waste biomass using TGA/DTG/MS. *Thermochim. Acta* **2018**, *670*, 44–54. [CrossRef]
33. Al bkoor Alrawashdeh, K.; Slopiecka, K.; Alshorman, A.A.; Bartocci, P.; Fantozzi, F. Pyrolytic degradation of Olive Waste Residue (OWR) by TGA: Thermal decomposition behavior and kinetic study. *J. Energy Power Eng.* **2017**, *11*, 497–510. [CrossRef]
34. Castells, B.; Varela, A.; Castillo-Ruiz, F.J.; Calvo, L.F.; Medic, L.; Tascón, A. Ignition and explosion characteristics of olive-derived biomasses. *Powder Technol.* **2023**, *420*, 118386. [CrossRef]
35. Orfão, J.J.M.; Antunes, F.J.A.; Figueiredo, J.L. Pyrolysis kinetics of lignocellulosic materials—Three independent reactions model. *Fuel* **1999**, *78*, 349–358. [CrossRef]
36. Anca-Couce, A.; Berger, A.; Zobel, N. How to determine consistent biomass pyrolysis kinetics in a parallel reaction scheme. *Fuel* **2014**, *123*, 230–240. [CrossRef]
37. Perejón, A.; Sánchez-Jiménez, P.E.; Criado, J.M.; Pérez-Maqueda, L.A. Kinetic analysis of complex solid-state reactions. A new deconvolution procedure. *J. Phys. Chem. B* **2011**, *115*, 1780–1791. [CrossRef]
38. Hu, M.; Chen, Z.; Wang, S.; Guo, D.; Ma, C.; Zhou, Y.; Chen, J.; Laghari, M.; Fazal, S.; Xiao, B.; et al. Thermogravimetric kinetics of lignocellulosic biomass slow pyrolysis using distributed activation energy model, Fraser–Suzuki deconvolution, and iso-conversional method. *Energy Convers. Manag.* **2016**, *118*, 1–11. [CrossRef]
39. Luo, G.; Wang, W.; Zhao, Y.; Tao, X.; Xie, W.; Wang, K. Autothermal pyrolysis of lignocellulosic biomass: Experimental, kinetic, and thermodynamic studies. *J. Anal. Appl. Pyrolysis* **2023**, *171*, 105972. [CrossRef]
40. Portarapillo, M.; Pietraccini, M.; Sanchirico, R.; Di Benedetto, A.; Dufaud, O. Investigation of the flash pyrolysis of biomass dust: Is there a correlation between MIT, volatile point and LFL of the pyrolysis gases? In Proceedings of the 15th International Symposium on Hazards, Prevention and Mitigation of Industrial Explosions (ISHPMIE 2024), Naples, Italy, 10–14 June 2024.
41. Greco, G.; Videgain, M.; Di Stasi, C.; González, B.; Manyà, J.J. Evolution of the mass-loss rate during atmospheric and pressurized slow pyrolysis of wheat straw in a bench-scale reactor. *J. Anal. Appl. Pyrolysis* **2018**, *136*, 18–26. [CrossRef]
42. Li, M.; Zhang, Y.S.; Cheng, S.; Qu, B.; Li, A.; Meng, F.; Ji, G. The impact of heating rate on the decomposition kinetics and product distribution of algal waste pyrolysis with in-situ weight measurement. *Chem. Eng. J.* **2023**, *457*, 141368. [CrossRef]
43. Aniza, R.; Chen, W.-H.; Kwon, E.E.; Bach, Q.V.; Hoang, A.T. Lignocellulosic biofuel properties and reactivity analyzed by thermogravimetric analysis (TGA) toward zero carbon scheme: A critical review. *Energy Convers. Manag. X* **2024**, *22*, 100538. [CrossRef]
44. Anca-Couce, A.; Tsekos, C.; Retschitzegger, S.; Zimbardi, F.; Funke, A.; Banks, S.; Kraia, T.; Marques, P.; Scharler, R.; de Jong, W.; et al. Biomass pyrolysis TGA assessment with an international round robin. *Fuel* **2020**, *276*, 118002. [CrossRef]
45. Riaz, S.; Oluwoye, I.; Al-Abdeli, Y.M. Oxidative torrefaction of densified woody biomass: Performance, combustion kinetics and thermodynamics. *Renew. Energy* **2022**, *199*, 908–918. [CrossRef]
46. Xu, X.; Pan, R.; Chen, R. Combustion Characteristics, Kinetics, and Thermodynamics of Pine Wood Through Thermogravimetric Analysis. *Appl. Biochem. Biotechnol.* **2021**, *193*, 1427–1446. [CrossRef] [PubMed]
47. Morgan, P.A.; Robertson, S.D.; Unsworth, J.F. Combustion studies by thermogravimetric analysis. *Fuel* **1986**, *65*, 1546–1551. [CrossRef]
48. *ASTM D3302-02*; Standard Test Method for Total Moisture in Coal. ASTM International: West Conshohocken, PA, USA, 2002.
49. *UNE 32019:1984*; Hard Coal and Coke. Determination of Volatile Matter Content. AENOR: Madrid, Spain, 1984.
50. *UNE 32004:1984*; Solid Mineral Fuels. Determination of Ash. AENOR: Madrid, Spain, 1984.
51. *ASTM D5373-21*; Standard Test Methods for Determination of Carbon, Hydrogen and Nitrogen in Analysis Samples of Coal and Carbon in Analysis Samples of Coal and Coke. ASTM International: West Conshohocken, PA, USA, 2021.
52. *ASTM D4239-18e1*; Standard Test Method for Sulfur in the Analysis Sample of Coal and Coke Using High-Temperature Tube Furnace Combustion. ASTM International: West Conshohocken, PA, USA, 2021.
53. *ASTM D2361-95*; Standard Test Method for Chlorine in Coal. ASTM International: West Conshohocken, PA, USA, 2021.
54. *UNE 32006:1995*; Solid Mineral Fuels. Determination of Gross Calorific Value by Automoatic Calorimeter. AENOR: Madrid, Spain, 1995.
55. Bitra, V.S.P.; Womac, A.R.; Chevanan, N.; Sokhansanj, S. Comminution Properties of Biomass in Hammer Mill and its Particle Size Characterization. In Proceedings of the 2008 Providence, Providence, RI, USA, 29 June–2 July 2008; American Society of Agricultural and Biological Engineers: St. Joseph, MI, USA, 2008.
56. Guo, Q.; Chen, X.; Liu, H. Experimental research on shape and size distribution of biomass particle. *Fuel* **2012**, *94*, 551–555. [CrossRef]
57. Castells, B.; Tascón, A.; Amez, I.; Fernandez-Anez, N. Influence of Particle Size on the Flammability and Explosibility of Biomass Dusts: Is a New Approach Needed? *Fire Technol.* **2023**, *59*, 2989–3025. [CrossRef]
58. Varela, A.; Castillo-Ruiz, F.J.; Arbizu-Milagro, J.; Tascón, A. The influence of moisture on the sieving performance of lignocellulosic biomass. *Biofuels Bioprod. Biorefin.* **2023**, *17*, 1708–1723. [CrossRef]
59. Alvarado Flores, J.J.; Rutiaga Quiñones, J.G. Estudio de cinética en procesos termogravimétricos de materiales lignocelulósicos. *Maderas Cienc. Y Tecnol.* **2018**, *20*, 221–238. [CrossRef]

60. Manals, E.; Penedo, M.; Ortega, G. Thermogravimetric and Thermal Analysis Differential Different Vegetable Biomasses. *Chem. Technol.* **2011**, *20*, 180–190.
61. Torrent, J.G.; Ramírez-Gómez, Á.; Fernandez-Anez, N.; Pejic, L.M.; Tascón, A. Influence of the composition of solid biomass in the flammability and susceptibility to spontaneous combustion. *Fuel* **2016**, *184*, 503–511. [CrossRef]
62. Chen, T.; Wu, W.; Wu, J.; Cai, J.; Wu, J. Determination of the pseudocomponents and kinetic analysis of selected combustible solid wastes pyrolysis based on Weibull model. *J. Therm. Anal. Calorim.* **2016**, *126*, 1899–1909. [CrossRef]
63. Li, Z.; Zhao, W.; Meng, B.; Liu, C.; Zhu, Q.; Zhao, G. Kinetic study of corn straw pyrolysis: Comparison of two different three-pseudocomponent models. *Bioresour. Technol.* **2008**, *99*, 7616–7622. [CrossRef] [PubMed]
64. Kim, H.; Yu, S.; Kim, M.; Ryu, C. Progressive deconvolution of biomass thermogram to derive lignocellulosic composition and pyrolysis kinetics for parallel reaction model. *Energy* **2022**, *254*, 124446. [CrossRef]
65. Ferreira, A.F.; Ferreira, A.; Dias, A.P.S.; Gouveia, L. Pyrolysis of Scenedesmus obliquus Biomass Following the Treatment of Different Wastewaters. *Bioenergy Res.* **2020**, *13*, 896–906. [CrossRef]
66. Rego, F.; Dias, A.P.S.; Casquilho, M.; Rosa, F.C.; Rodrigues, A. Fast determination of lignocellulosic composition of poplar biomass by thermogravimetry. *Biomass Bioenergy* **2019**, *122*, 375–380. [CrossRef]
67. Naya, S.; Cao, R.; de Ullibarri, I.L.; Artiaga, R.; Barbadillo, F.; García, A. Logistic mixture model versus Arrhenius for kinetic study of material degradation by dynamic thermogravimetric analysis. *J. Chemom.* **2006**, *20*, 158–163. [CrossRef]
68. Chen, C.; Miao, W.; Zhou, C.; Wu, H. Thermogravimetric pyrolysis kinetics of bamboo waste via Asymmetric Double Sigmoidal (Asym2sig) function deconvolution. *Bioresour. Technol.* **2017**, *225*, 48–57. [CrossRef]
69. Castells, B.; Amez, I.; Medic, L.; García-Torrent, J. Torrefaction influence on combustion kinetics of Malaysian oil palm wastes. *Fuel Process. Technol.* **2021**, *218*, 106843. [CrossRef]
70. Cheng, Z.; Wu, W.; Ji, P.; Zhou, X.; Liu, R.; Cai, J. Applicability of Fraser–Suzuki function in kinetic analysis of DAEM processes and lignocellulosic biomass pyrolysis processes. *J. Therm. Anal. Calorim.* **2015**, *119*, 1429–1438. [CrossRef]
71. Bilkic, B.; Haykiri-Acma, H.; Yaman, S. Combustion reactivity estimation parameters of biomass compared with lignite based on thermogravimetric analysis. *Energy Sources Part A Recover. Util. Environ. Eff.* **2023**, *45*, 370–383. [CrossRef]
72. Qin, Z.; Lei, M.; Zhang, L. Thermogravimetric analysis of the co-combustion of bituminous coal, rice straw and sewage sludge. *IOP Conf. Ser. Earth Environ. Sci.* **2022**, *1011*, 012028. [CrossRef]
73. Wang, Z.; Hong, C.; Xing, Y.; Li, Y.; Feng, L.; Jia, M. Combustion behaviors and kinetics of sewage sludge blended with pulverized coal: With and without catalysts. *Waste Manag.* **2018**, *74*, 288–296. [CrossRef] [PubMed]
74. Mureddu, M.; Dessì, F.; Orsini, A.; Ferrara, F.; Pettinau, A. Air- and oxygen-blown characterization of coal and biomass by thermogravimetric analysis. *Fuel* **2018**, *212*, 626–637. [CrossRef]
75. Kumar, R.; Singh, R.I. An investigation of co-combustion municipal sewage sludge with biomass in a 20 kW BFB combustor under air-fired and oxygen-enriched condition. *Waste Manag.* **2017**, *70*, 114–126. [CrossRef] [PubMed]
76. Apaydin-Varol, E.; Polat, S.; Putun, A. Pyrolysis kinetics and thermal decomposition behavior of polycarbonate—A TGA-FTIR study. *Therm. Sci.* **2014**, *18*, 833–842. [CrossRef]
77. Garcia, E.; Ejim, I.F.; Liu, H. Thermogravimetric analysis of co-combustion of a bituminous coal and coffee industry by-products. *Thermochim. Acta* **2022**, *715*, 179296. [CrossRef]
78. Liu, Y.; Cao, X.; Duan, X.; Wang, Y.; Che, D. Thermal analysis on combustion characteristics of predried dyeing sludge. *Appl. Therm. Eng.* **2018**, *140*, 158–165. [CrossRef]
79. Sieradzka, M.; Gao, N.; Quan, C.; Mlonka-Mędrala, A.; Magdziarz, A. Biomass Thermochemical Conversion via Pyrolysis with Integrated CO_2 Capture. *Energies* **2020**, *13*, 1050. [CrossRef]
80. Castells, B.; Amez, I.; Manić, N.G.; Stojiljković, D.D.; Medic, L.; Garcia-Torrent, J. Kinetic study of different biomass pyrolysis and oxygen-enriched combustion. *Therm. Sci.* **2022**, *26*, 4131–4145. [CrossRef]
81. Friedman, H.L. Kinetics of thermal degradation of char-forming plastics from thermogravimetry. Application to a phenolic plastic. *J. Polym. Sci. Part C Polym. Symp.* **1964**, *6*, 183–195. [CrossRef]
82. Kissinger, H.E. Reaction Kinetics in Differential Thermal Analysis. *Anal. Chem.* **1957**, *29*, 1702–1706. [CrossRef]
83. Flynn, J.H.; Wall, L.A. A quick, direct method for the determination of activation energy from thermogravimetric data. *J. Polym. Sci. B* **1966**, *4*, 323–328. [CrossRef]
84. Zaker, A.; Chen, Z.; Zaheer-Uddin, M.; Guo, J. Co-pyrolysis of sewage sludge and low-density polyethylene—A thermogravimetric study of thermo-kinetics and thermodynamic parameters. *J. Environ. Chem. Eng.* **2021**, *9*, 104554. [CrossRef]
85. Naqvi, S.R.; Hameed, Z.; Tariq, R.; Taqvi, S.A.; Ali, I.; Niazi, M.B.K.; Noor, T.; Hussain, A.; Iqbal, N.; Shahbaz, M. Synergistic effect on co-pyrolysis of rice husk and sewage sludge by thermal behavior, kinetics, thermodynamic parameters and artificial neural network. *Waste Manag.* **2019**, *85*, 131–140. [CrossRef] [PubMed]
86. Maestri, D.; Barrionuevo, D.; Bodoira, R.; Zafra, A.; Jiménez-López, J.; Alché, J.d.D. Nutritional profile and nutraceutical components of olive (*Olea europaea* L.) seeds. *J. Food Sci. Technol.* **2019**, *56*, 4359–4370. [CrossRef] [PubMed]
87. Subramanian, S.; Reddy Ragula, U.B. Pyrolysis kinetics of *Hibiscus rosa sinensis* and *Nerium oleander*. *Biofuels* **2020**, *11*, 903–917. [CrossRef]
88. Manić, N.; Janković, B.; Stojiljković, D.; Radojević, M.; Somoza, B.C.; Medić, L. Self-ignition potential assessment for different biomass feedstocks based on the dynamic thermal analysis. *Clean. Eng. Technol.* **2021**, *2*, 100040. [CrossRef]

89. Ma, Z.; Chen, D.; Gu, J.; Bao, B.; Zhang, Q. Determination of pyrolysis characteristics and kinetics of palm kernel shell using TGA–FTIR and model-free integral methods. *Energy Convers. Manag.* **2015**, *89*, 251–259. [CrossRef]
90. Manic, N.G.; Jankovic, B.Z.; Stojiljkovic, D.D.; Jovanovic, V.V.; Radojevic, M.B. TGA-DSC-MS analysis of pyrolysis process of various agricultural residues. *Therm. Sci.* **2019**, *23*, 1457–1472. [CrossRef]
91. Carrier, M.; Auret, L.; Bridgwater, A.; Knoetze, J.H. Using Apparent Activation Energy as a Reactivity Criterion for Biomass Pyrolysis. *Energy Fuels* **2016**, *30*, 7834–7841. [CrossRef]
92. Sukiran, M.A.; Abnisa, F.; Daud, W.M.A.W.; Abu Bakar, N.; Loh, S.K. A review of torrefaction of oil palm solid wastes for biofuel production. *Energy Convers. Manag.* **2017**, *149*, 101–120. [CrossRef]
93. Svoboda, R.; Málek, J. Applicability of Fraser–Suzuki function in kinetic analysis of complex crystallization processes. *J. Therm. Anal. Calorim.* **2013**, *111*, 1045–1056. [CrossRef]
94. Grønli, M.G.; Várhegyi, G.; Di Blasi, C. Thermogravimetric Analysis and Devolatilization Kinetics of Wood. *Ind. Eng. Chem. Res.* **2002**, *41*, 4201–4208. [CrossRef]
95. Rusanen, A.; Lappalainen, K.; Kärkkäinen, J.; Tuuttila, T.; Mikola, M.; Lassi, U. Selective hemicellulose hydrolysis of Scots pine sawdust. *Biomass Convers. Biorefin.* **2019**, *9*, 283–291. [CrossRef]
96. Shang, L.; Nielsen, N.P.K.; Dahl, J.; Stelte, W.; Ahrenfeldt, J.; Holm, J.K.; Thomsen, T.; Henriksen, U.B. Quality effects caused by torrefaction of pellets made from Scots pine. *Fuel Process. Technol.* **2012**, *101*, 23–28. [CrossRef]
97. Zborowska, M.; Prądzyński, W.; Kusiak, W.; Stachowiak-Wencek, A.; Roszyk, E.; Moliński, W. A Selection of the application of *Pinus Sylvestris* L. from puszcza notecka by chemical analysis. *Drew. Pr. Nauk. Doniesienia Komun. Wood Res. Pap. Rep. Announc.* **2018**, *61*, 39–51. [CrossRef]
98. Lühr, C.; Pecenka, R. Development of a model for the fast analysis of polymer mixtures based on cellulose, hemicellulose (xylan), lignin using thermogravimetric analysis and application of the model to poplar wood. *Fuel* **2020**, *277*, 118169. [CrossRef]
99. Sun, S.-C.; Wang, P.-F.; Cao, X.-F.; Wen, J.-L. An integrated pretreatment for accelerating the enzymatic hydrolysis of poplar and improving the isolation of co-produced hemicelluloses. *Ind. Crop. Prod.* **2021**, *173*, 114101. [CrossRef]
100. Huang, Y.; Liu, H.; Yuan, H.; Zhan, H.; Zhuang, X.; Yuan, S.; Yin, X.; Wu, C. Relevance between chemical structure and pyrolysis behavior of palm kernel shell lignin. *Sci. Total Environ.* **2018**, *633*, 785–795. [CrossRef]
101. Gul, E.; Alrawashdeh, K.A.B.; Masek, O.; Skreiberg, Ø.; Corona, A.; Zampilli, M.; Wang, L.; Samaras, P.; Yang, Q.; Zhou, H.; et al. Production and use of biochar from lignin and lignin-rich residues (such as digestate and olive stones) for wastewater treatment. *J. Anal. Appl. Pyrolysis* **2021**, *158*, 105263. [CrossRef]
102. Cequier, E.; Aguilera, J.; Balcells, M.; Canela-Garayoa, R. Extraction and characterization of lignin from olive pomace: A comparison study among ionic liquid, sulfuric acid, and alkaline treatments. *Biomass Convers. Biorefin.* **2019**, *9*, 241–252. [CrossRef]
103. Sandouqa, A.; Al-Hamamre, Z.; Asfar, J. Preparation and performance investigation of a lignin-based solid acid catalyst manufactured from olive cake for biodiesel production. *Renew. Energy* **2019**, *132*, 667–682. [CrossRef]
104. Portarapillo, M.; Danzi, E.; Sanchirico, R.; Marmo, L.; Di Benedetto, A. Energy Recovery from Vinery Waste: Dust Explosion Issues. *Appl. Sci.* **2021**, *11*, 11188. [CrossRef]
105. Wzorek, M.; Junga, R.; Yilmaz, E.; Bozhenko, B. Thermal Decomposition of Olive-Mill Byproducts: A TG-FTIR Approach. *Energies* **2021**, *14*, 4123. [CrossRef]
106. Afessa, M.M.; Ramayya, A.V.; Nega, D.T.; Mossisa, H.M.; Locaspi, A.; Faravelli, T.F. Investigation of Kinetic, Thermodynamic and Performance Parameters during Devolatilization of Agricultural biomass Waste via TGA. *Ethiop. J. Appl. Sci. Technol.* **2023**, 16–24.
107. Menzinger, M.; Wolfgang, R. The Meaning and Use of the Arrhenius Activation Energy. *Angew. Chem. Int. Ed. Engl.* **1969**, *8*, 438–444. [CrossRef]
108. Radojević, M.; Janković, B.; Jovanović, V.; Stojiljković, D.; Manić, N. Comparative pyrolysis kinetics of various biomasses based on model-free and DAEM approaches improved with numerical optimization procedure. *PLoS ONE* **2018**, *13*, e0206657. [CrossRef]
109. Jiang, L.; Yang, X.-R.; Gao, X.; Xu, Q.; Das, O.; Sun, J.-H.; Kuzman, M.K. Pyrolytic Kinetics of Polystyrene Particle in Nitrogen Atmosphere: Particle Size Effects and Application of Distributed Activation Energy Method. *Polymers* **2020**, *12*, 421. [CrossRef]
110. Cui, Z.; Xue, Y.; Xiao, L.; Wang, T. Effect of Particle Size on Activation Energy for Thermal Decomposition of Nano-$CaCO_3$. *J. Comput. Theor. Nanosci.* **2013**, *10*, 569–572. [CrossRef]
111. Özveren, U.; Özdoğan, Z.S. Investigation of the slow pyrolysis kinetics of olive oil pomace using thermo-gravimetric analysis coupled with mass spectrometry. *Biomass Bioenergy* **2013**, *58*, 168–179. [CrossRef]
112. Xiang, Y.; Xiang, Y.; Wang, L. Kinetics of the thermal decomposition of poplar sawdust. *Energy Sources Part A Recover. Util. Environ. Eff.* **2017**, *39*, 213–218. [CrossRef]
113. Sharma, A.; Aravind Kumar, A.; Mohanty, B.; Sawarkar, A.N. Critical insights into pyrolysis and co-pyrolysis of poplar and eucalyptus wood sawdust: Physico-chemical characterization, kinetic triplets, reaction mechanism, and thermodynamic analysis. *Renew. Energy* **2023**, *210*, 321–334. [CrossRef]
114. Gu, X.; Liu, C.; Jiang, X.; Ma, X.; Li, L.; Cheng, K.; Li, Z. Thermal behavior and kinetics of the pyrolysis of the raw/steam exploded poplar wood sawdust. *J. Anal. Appl. Pyrolysis* **2014**, *106*, 177–186. [CrossRef]
115. Xu, L.; Zhou, J.; Ni, J.; Li, Y.; Long, Y.; Huang, R. Investigating the pyrolysis kinetics of Pinus sylvestris using thermogravimetric analysis. *Bioresources* **2020**, *15*, 5577–5592. [CrossRef]
116. Mishra, G.; Kumar, J.; Bhaskar, T. Kinetic studies on the pyrolysis of pinewood. *Bioresour. Technol.* **2015**, *182*, 282–288. [CrossRef]

117. Xiao, R.; Yang, W.; Cong, X.; Dong, K.; Xu, J.; Wang, D.; Yang, X. Thermogravimetric analysis and reaction kinetics of lignocellulosic biomass pyrolysis. *Energy* **2020**, *201*, 117537. [CrossRef]
118. Rego, F.; Dias, A.P.S.; Casquilho, M.; Rosa, F.C.; Rodrigues, A. Pyrolysis kinetics of short rotation coppice poplar biomass. *Energy* **2020**, *207*, 118191. [CrossRef]
119. Quesada, L.; Pérez, A.; Calero, M.; Blázquez, G.; Martín-Lara, M. Kinetic study of thermal degradation of olive cake based on a scheme of fractionation and its behavior impregnated of metals. *Bioresour. Technol.* **2018**, *261*, 104–116. [CrossRef]
120. Asimakidou, T.; Chrissafis, K. Thermal behavior and pyrolysis kinetics of olive stone residue. *J. Therm. Anal. Calorim.* **2022**, *147*, 9045–9054. [CrossRef]
121. Slopiecka, K.; Bartocci, P.; Fantozzi, F. Thermogravimetric analysis and kinetic study of poplar wood pyrolysis. *Appl. Energy* **2012**, *97*, 491–497. [CrossRef]
122. Patidar, K.; Singathia, A.; Vashishtha, M.; Sangal, V.K.; Upadhyaya, S. Investigation of kinetic and thermodynamic parameters approaches to non-isothermal pyrolysis of mustard stalk using model-free and master plots methods. *Mater. Sci. Energy Technol.* **2022**, *5*, 6–14. [CrossRef]
123. Carvalho, M.; Oliveira, A.P.; Mayer, F.; Virgens, C.; Rangel, M.D.C. Thermokinetic and Thermodynamic Parameters for Catalytic Pyrolysis of Medium Density Fiber over Ni/Beta Zeolite. *Catal. Res.* **2022**, *2*, 038. [CrossRef]
124. Fan, F.; Zheng, Y.; Huang, Y.; Lu, Y.; Wang, Z.; Chen, B.; Zheng, Z. Combustion Kinetics of Biochar Prepared by Pyrolysis of Macadamia Shells. *Bioresources* **2017**, *12*, 3918–3932. [CrossRef]
125. Sánchez-Ávila, N.; Cardarelli, A.; Carmona-Cabello, M.; Dorado, M.; Pinzi, S.; Barbanera, M. Kinetic and thermodynamic behavior of co-pyrolysis of olive pomace and thermoplastic waste via thermogravimetric analysis. *Renew. Energy* **2024**, *230*, 120880. [CrossRef]
126. Chaula, Z.; John, G.; Said, M.; Manyele, S.; Mhilu, C. Non-Isothermal Degradation and Thermodynamic Properties of Pine Sawdust. *Smart Grid Renew. Energy* **2018**, *9*, 272–284. [CrossRef]

Disclaimer/Publisher's Note: The statements, opinions and data contained in all publications are solely those of the individual author(s) and contributor(s) and not of MDPI and/or the editor(s). MDPI and/or the editor(s) disclaim responsibility for any injury to people or property resulting from any ideas, methods, instructions or products referred to in the content.